ICARUS 20, 322–345 (1973)

On the Reduction of Occultation Light Curves

L. WASSERMAN AND J. VEVERKA

Laboratory for Planetary Studies, Center for Radiophysics and Space Research, Cornell University, Ithaca, New York 14850

Received May 10, 1973; revised June 7, 1973

In the first two sections of this paper, the two basic methods of reducing occultation light curves—curve fitting and inversion—are reviewed and compared. It is shown that the curve fitting methods have severe problems of nonuniqueness. In addition, in the case of occultation curves dominated by spikes, it is not clear that such solutions are meaningful. The inversion method does not suffer from these drawbacks. Methods of deriving temperature profiles from refractivity profiles are dealt with in the third section. It is shown that, although the temperature profiles are sensitive to small errors in the refractivity profile, accurate temperatures can be obtained, particularly at the deeper levels of the atmosphere. The final section contains a brief discussion of the ambiguities that arise when the occultation curve straddles the turbopause.

INTRODUCTION

Occultations of bright stars by planets provide important information about planetary upper atmospheres. By observing the rate of change of the star's brightness as it is occulted, the refractivity as a function of height in the planet's upper atmosphere can be determined. To date, four planetary occultations have been observed successfully: σ Arietis by Jupiter (Baum and Code, 1953), Regulus by Venus (de Vaucouleurs and Menzel, 1960), BD -17° 4388 by Neptune (Freeman and Lyngå, 1970; and others), and Beta Scorpii by Jupiter (Veverka *et al.*, 1971; Hubbard *et al.*, 1972; and others).

The details of a typical occultation of a star by a planet are discussed by Baum and Code (1953) and depicted schematically in Fig. 1. As the star is occulted by the planet, its rate of disappearance is determined by the spreading of its light due to differential refraction; ordinary extinction effects are negligible. The total bending of a light ray, $\theta(r_1)$, whose closest approach to the center of the planet is r_1, is given by

$$\theta(r_1) = \int_{-\infty}^{+\infty} \left(\frac{1}{n} \cdot \frac{dn}{dr}\right) \cdot dx \simeq \int_{-\infty}^{+\infty} \frac{d\nu}{dr} \cdot dx \quad (1)$$

Here $n = n(r)$ is the index of refraction at level r, $\nu = n - 1$ is the refractivity, and dx is an increment of path length along the direction of the ray (θ is assumed to be small). The resulting occultation curve is given by

$$(\phi^*/\phi) - 1 = D(d\theta/dr) \quad (2)$$

where ϕ^* = unocculted star flux, $\phi = \phi(t)$ = star flux at time t, and D = Earth–planet distance. The parameters are defined such that r increases upwards, ν is everywhere positive and increases inwards, θ is everywhere negative, and $|\theta|$ increases inwards. Therefore, $d\nu/dr$ is negative and $d\theta/dr$ is positive.

Two different methods are available for deriving information about atmospheric structure from occultation curves. First, an atmospheric profile can be assumed (one specifies ν as a function of r), and a synthetic occultation curve is calculated which is then compared with the observed curve. The refractivity profile is varied until a match which is considered satisfactory is obtained. This procedure has been adopted commonly in the past, but only for restricted classes of $\nu(r)$: for isothermal, homogeneous, constant scale height atmospheres (Baum and Code, 1953; Freeman and Lyngå, 1970), and for similar linear temperature gradient atmospheres (Gold-

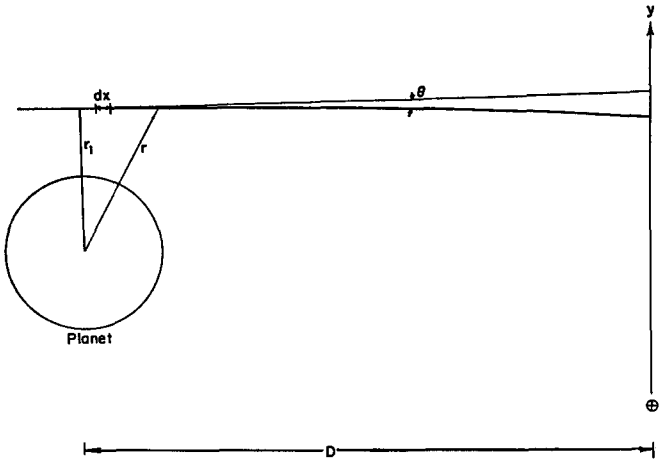

FIG. 1. Schematic occultation scene. The frame of reference is such that the planet is stationary and the observer moves with velocity $-v$. The ray shown is bent by total amount θ, and its closest point of approach to the center of the planet is r_1.

smith, 1963; de Vaucouleurs and Menzel, 1960).

The second method for occultation light curve reduction uses the fact that $d\theta/dr$ can be determined directly from the observations. Then, $\nu(r)$ can be obtained from (1) by inverting this integral equation. This method has been used successfully by Kovalevsky and Link, (1969) and by Hubbard *et al.* (1972) in reducing occultation light curves and by Fjeldbo and his coworkers in reducing spacecraft radio occultation data (see for example, Fjeldbo, Kliore, and Eshleman, 1971).

In occultation light curve work, the first method has been used more frequently than the second (in addition to references above, see Freeman and Stokes, 1972; Larson, 1972), probably because its application is computationally trivial. However, as we shall show, in the case of occultation light curves containing spikes, this method cannot be applied meaningfully, and attempts to do so lead to deceptive results. Therefore, this approach must be avoided in such cases.

PART I. FIRST METHOD: CURVE FITTING

1. *Spikeless Occultation Curves: Effects of Noise*

Given the density structure of a well-mixed atmosphere, the problem is to derive the occultation light curve, which is to be compared with the observed occultation curve. The density structure is altered until a satisfactory match between the calculated and the observed curves is obtained. Although this method has been applied frequently in the past, no discussion of the effects of noise has been given. Therefore, we begin by considering this question.

For simplicity, we will deal only with homogeneous, isothermal, constant scale height atmospheres. This case is of special relevance since it has been used commonly in past analyses of occultation light curves.

In the absence of noise, for an isothermal atmosphere with scale height:

$$H = RT/\mu g,$$

the resulting occultation light curve is given by the "Baum and Code" (1953) equation:

$$\frac{v(t - t_0)}{H} = \left(\frac{\phi^*}{\phi} - 2\right) + \ln\left(\frac{\phi^*}{\phi} - 1\right) \quad (3)$$

where

v = speed of the observer relative to the planet's limb. The planet is assumed stationary, and the observer moves in the $-y$ direction (Fig. 1),

t_0 = "time of occultation" = time for which $\phi = \phi^*/2$,

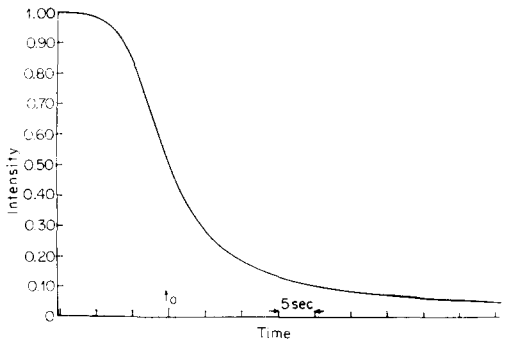

FIG. 2. Model light curve. Isothermal atmosphere $v/H = 0.5\,\mathrm{sec}^{-1}$.

g = acceleration due to gravity (assumed constant),
μ = mean molecular weight of atmosphere (assumed constant),
T = temperature of isothermal atmosphere, and
R = universal gas constant.

The quantities ϕ and ϕ^* have been previously defined in connection with Eq. (2).

We now consider how the comparison between a calculated occultation curve and an observed curve is affected by the presence of noise. To make the discussion concrete we deal with a particular, representative case: a Baum and Code occultation curve for which $v/H = 0.5\,\mathrm{sec}^{-1}$. The theoretical curve for this case (Eq. 3) is plotted in Fig. 2 from $(t - t_0,\ \phi/\phi^*) = (-15,\ 0.999)$ to $(t - t_0,\ \phi/\phi^*) = (45,\ 0.046)$, t being given in seconds.

The simplest way of obtaining v/H from such a curve is to plot the quantity

$$[(\phi^*/\phi) - 2) + \ln[(\phi^*/\phi) - 1] \equiv B(\phi^*/\phi)$$

against t. The result will be a straight line with slope v/H, which crosses the horizontal axis at $t = t_0$ (the "time of the occultation"). Noise tends to make the fitted straight line steeper; that is, it increases the inferred value of v/H. However, since the effects of noise on $B(\phi^*/\phi)$ are different at the two ends of the range of the function (Fig. 3), the fit is much more sensitive to noise on the tail of the light curve where $B(\phi^*/\phi)$ goes to infinity as $1/X$ as $X \equiv \phi/\phi^* \to 0$ than on the shoulder, where it goes to minus infinity as $\ln X$ as $X \to 1$.

Artificial noise was superimposed on the curve shown in Fig. 2, by generating random numbers having a Gaussian distribution with zero mean value, and standard deviation σ. For each value of σ, five different runs were made.

For the reasons given above, in using the straight line method, points near $X = 0$ and $X = 1$ should be avoided. To emphasize this, we have carried out two sets of calculations for the artificially noisy $v/H =$

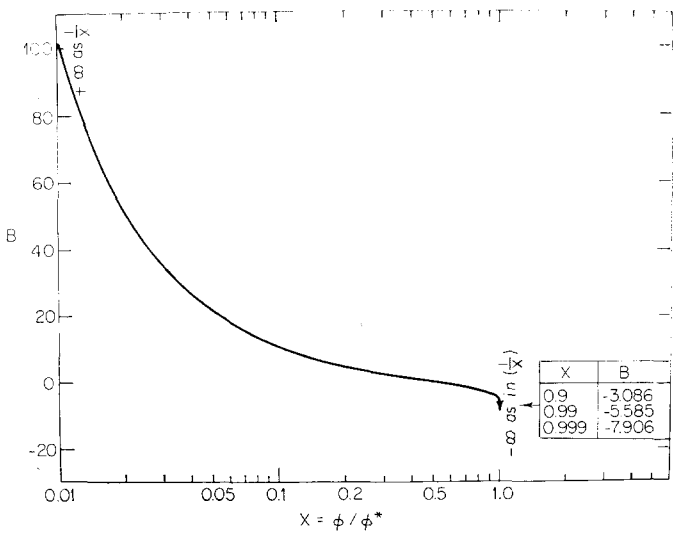

FIG. 3. Behaviour of the Baum and Code function $B(X)$ as a function of X.

TABLE I

EFFECTS OF NOISE: STRAIGHT-LINE FIT ($0.999 \geqslant X \geqslant 0.01$)[a]

Noise level		Fitted parameters				
		Trial 1	Trial 2	Trial 3	Trial 4	Trial 5
$\sigma = 0.0$	v/H	0.500				
	t_0	0.0				
	R	1.0				
$\sigma = 0.005$	v/H	0.599	0.871	0.636	0.724	1.376
	t_0	3.98	16.97	9.22	13.01	27.02
	R	0.686	0.315	0.615	0.623	0.185
$\sigma = 0.010$	v/H	0.970	1.232	1.408	0.758	0.843
	t_0	15.09	19.22	27.89	4.95	3.08
	R	0.209	0.281	0.176	0.432	0.235
$\sigma = 0.025$	v/H	1.543	0.778	1.546	0.654	0.612
	t_0	9.78	−16.17	25.53	−40.53	−13.8
	R	0.117	0.168	0.151	0.137	0.274

[a] R is the regression coefficient. Values of R close to unity indicate good fits; values much less than unity indicate poor fits.

$0.5\,\mathrm{sec}^{-1}$ data using the ranges ($0.999 \geqslant X \geqslant 0.01$) and ($0.9 \geqslant X \geqslant 0.1$), respectively. The fits were done by least squares. The results are given in Tables I and II.

From Table I ($0.999 \geqslant X \geqslant 0.01$) it is clear that, even in the presence of very small amounts of noise ($\sigma = 0.005$), extremely poor fits result. All fitted values of v/H are larger than the true value, as predicted above.

Reasonable results can be obtained by avoiding the shoulder and tail of the occultation curve and restricting the straight line fit to the range $0.9 \geqslant X \geqslant 0.1$ (Table II), but only if the noise level is low. For noise levels $\geqslant 5\%$, meaningful results cannot be expected. Usually, but not always, a large regression coefficient indicates a derived v/H close to the true value.

Another method of fitting the same type of data consists of finding the particular values of v/H and t_0 which, when inserted into Eq. (3), minimize the sum of the squares of the differences between the observed and calculated curves. This method has an important advantage over the previous one, since there is no undue difficulty with data points close to $X = 0$ or $X = 1$. Results of a noise analysis similar to that used in generating Tables I and II are shown in Table III. This method appears to give acceptable results even in the presence of large amounts of noise and appears to be preferable, in this respect, to the straight line method discussed previously.

This method is, however, sensitive to the choice of the zero and unity levels. This problem has been discussed by Hubbard *et al.* (1972).

2. *Occultation Curves with Spikes*

A common feature of many occultation curves is the presence of "spikes"—abrupt intensity flashes probably due to fluctuations in the atmospheric density structure (Freeman and Lyngå, 1970; Veverka *et al.*, 1971). A typical occultation light curve, for the emersion of β Sco AB (May 13, 1971) is shown in Fig. 4a, at a time resolution of 0.1 sec; also shown is the Fourier analysis of this curve using 10 to 600 terms (Figs. 4b–4g). Clearly the spikes represent the high frequency component of the data, but it cannot be true that they are ignorable from the point of view of determining atmospheric structure (as stated by Free-

TABLE II

EFFECTS OF NOISE: STRAIGHT-LINE FIT ($0.9 \geqslant X \geqslant 0.1$)

Noise level		Fitted parameters				
		Trial 1	Trial 2	Trial 3	Trial 4	Trial 5
$\sigma = 0.0$	v/H	0.5				
	t_0	0.0				
	R	1.0				
$\sigma = 0.005$	v/H	0.504	0.500	0.491	0.498	0.496
	t_0	0.03	0.01	0.02	−0.02	−0.03
	R	0.997	0.999	0.997	0.998	0.998
$\sigma = 0.025$	v/H	0.514	0.477	0.510	0.556	0.485
	t_0	0.01	−0.11	−0.22	−0.08	−0.33
	R	0.936	0.951	0.942	0.938	0.946
$\sigma = 0.050$	v/H	0.815	0.658	0.547	0.486	1.009
	t_0	0.16	−0.59	−0.28	−0.12	0.24
	R	0.738	0.689	0.806	0.922	0.345
$\sigma = 0.070$	v/H	0.476	0.948	0.661	0.506	0.539
	t_0	−0.63	−1.85	−0.56	−0.10	−0.11
	R	0.753	0.308	0.601	0.790	0.689
$\sigma = 0.090$	v/H	1.239	1.025	0.720	3.944	0.500
	t_0	−1.28	0.03	0.32	−1.25	−2.50
	R	0.270	0.328	0.732	0.162	0.565

man and Lyngå (1970), for example). Fitting a curve through the bottom of the spikes cannot give the true atmospheric profile since by conservation of photons the light in the spikes must come from somewhere. On the other hand, it is not clear that fitting a Baum and Code type curve to an occultation light curve by least squares is the answer. What is the meaning of such a "solution"? It is our impression that in the presence of spikes, occultation curves cannot be analyzed meaningfully by curve fitting; the inversion technique, described in Part II, must be used.

TABLE III

EFFECTS OF NOISE: LEAST-SQUARES FIT FOR v/H AND t_0

Noise level		Fitted parameters				
		Trial 1	Trial 2	Trial 3	Trial 4	Trial 5
$\sigma = 0.0$	v/H	0.50				
	t_0	0.0				
$\sigma = 0.025$	v/H	0.52	0.52	0.50	0.50	0.50
	t_0	0.1	−0.2	−0.1	0	0
$\sigma = 0.05$	v/H	0.50	0.46	0.52	0.50	0.54
	t_0	0.3	−0.1	−0.1	−0.1	0.1
$\sigma = 0.075$	v/H	0.46	0.52	0.48	0.48	0.50
	t_0	0.2	0.2	−0.3	0.3	−0.2

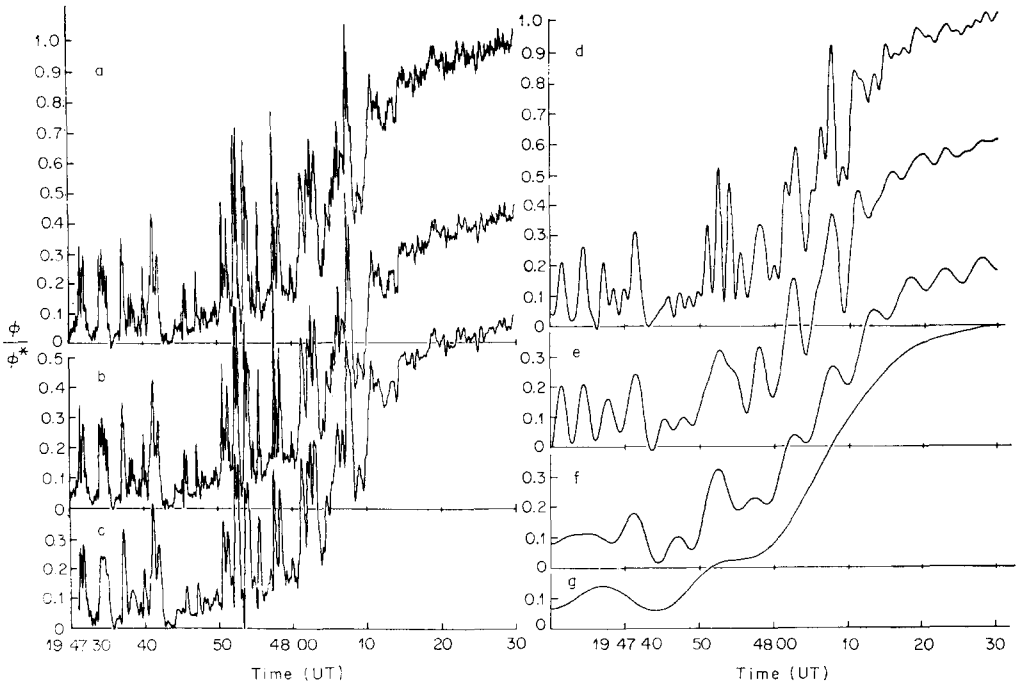

FIG. 4. Fourier analysis of an occultation curve. Shown are: (a) Observed light curve for the emersion of β Sco AB at 0.1 sec resolution. (b) Reconstructed curve using 600 Fourier components, (c) 300 components, (d) 100, (e) 50, (f) 25, and (g) 10 components.

3. *Uniqueness of Isothermal Solutions*

At this point we must briefly consider the uniqueness of the inferred atmospheric profiles. To simplify the discussion we will deal only with occultation curves totally free of spikes and noise. It is clear that the presence of noise will increase the difficulty of reconstructing the true atmospheric profile correctly.

Assuming that an isothermal fit to an observed (spikeless) occultation curve has been obtained, does this mean that the atmosphere is isothermal? The answer is definitely no, as was first shown explicitly by Goldsmith (1963), who considered atmospheres in which the temperature varies linearly with height, while the mean molecular weight remains constant. That is,

$$T(r) = T_0 + \Gamma(r - r_0)$$

and (4)

$$H(r) = H_0 + G(r - r_0)$$

where $\Gamma = dT/dr$ and $G = R\Gamma/\mu g$. The resulting occultation curve is given by,

$$\frac{v(t-t_0)}{H_0} = \frac{1}{(1+\frac{3}{2}G)} \times \left[\left(\frac{\phi^*}{\phi} - 1\right)^{(\gamma+3/2)/(\gamma+5/2)} - 1\right] + \frac{1}{G}\left[1 - \left(\frac{\phi^*}{\phi} - 1\right)^{-1/(\gamma+5/2)}\right] \tag{5}$$

where $\gamma \equiv 1/G$.

For $G \to 0$ this reduces to:

$$\frac{v(t-t_0)}{H_0} = \frac{1}{(1+\frac{3}{2}G)}\left[\left(\frac{\phi^*}{\phi} - 2\right) + \ln\left(\frac{\phi^*}{\phi} - 1\right)\right] \tag{6}$$

For $G = 0$ this is the Baum and Code equation (3). Equation (6) can be reduced to a Baum and Code form by setting

$$H = H_0/(1 + \tfrac{3}{2}G) \tag{7}$$

In other words, for G small, a linear temperature gradient atmosphere will produce an occultation light curve which looks like

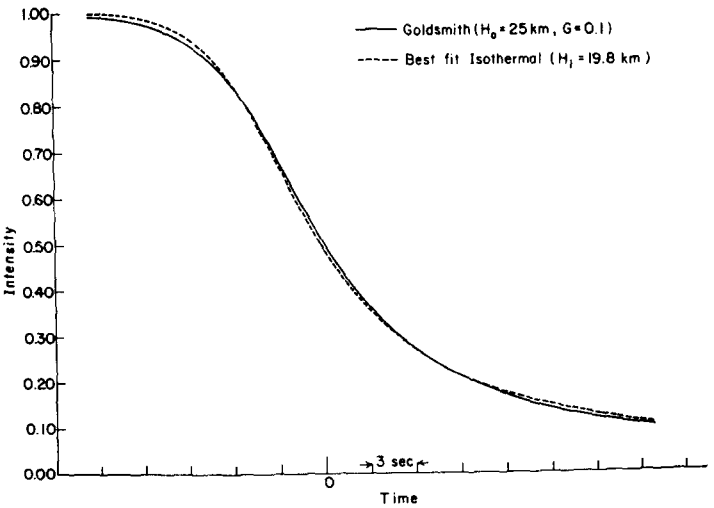

FIG. 5. Best isothermal fit to a Goldsmith linear scale height gradient atmosphere. ($H_0 = 25$km, $G = +0.1$).

that produced by an isothermal atmosphere of a different scale height. To illustrate this we have generated a series of occultation curves using Eq. (5) and the following parameters: $v = 8.5$km/sec; $H_0 = 25$km; $G = 0.1, -0.1$, and $+0.3$.

For each case, the best isothermal fit was found by varying H and t_0 to minimize the sum of the squares of the differences between the two curves. The results are shown in Figs. 5, 6, and 7. In each case, the isothermal fit agrees with the Goldsmith curve to within a few percent, and *in the presence of small amounts of random noise it would be impossible to notice a difference.* For instance, for the case shown in Fig. 5, a Goldsmith atmosphere with $H_0 = 25$km and $G = 0.1$ can be confused with an isothermal atmosphere with $H = 19.8$km. Equation (7) gives $H = 22$km, but this expression is only approximate for $G \neq 0$. For $G = 0.3$ (Fig. 7), $H = 14.4$km for the

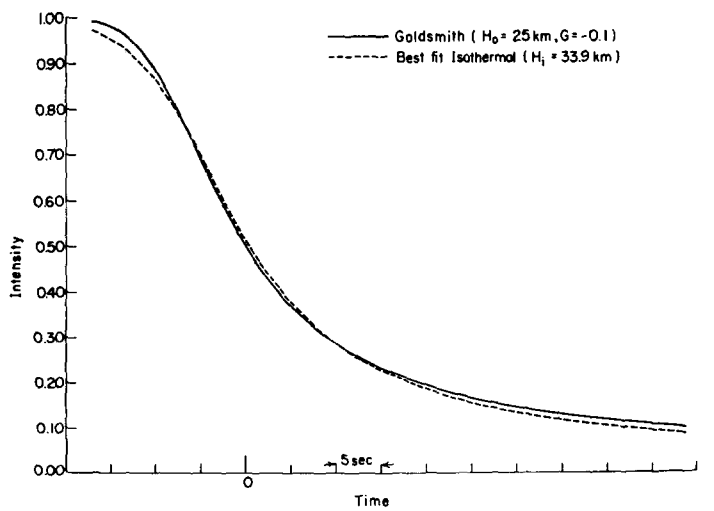

FIG. 6. Best isothermal fit to a Goldsmith linear scale height gradient atmosphere. ($H_0 = 25$km, $G = -0.1$.)

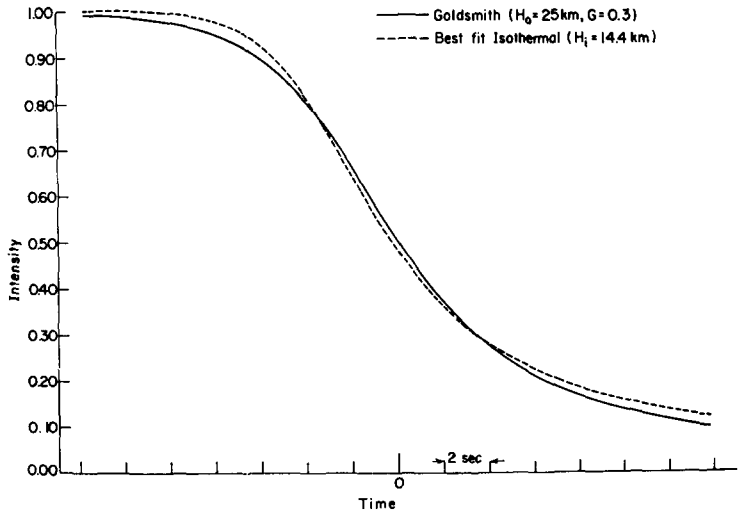

FIG. 7. Best isothermal fit to a Goldsmith linear scale height gradient atmosphere ($H_0 = 25$km, $G = +0.3$).

best isothermal fit; Eq. (7) predicts a value of 17.3km.

This illustrates one important ambiguity, first stressed by Goldsmith (1963), but ignored by many subsequent authors: the occultation curve of any specific isothermal atmosphere is for practical purposes indistinguishable from that of a family of constant gradient atmospheres.

More generally, it is often easy to find excellent isothermal fits to occultation light curves even when the true atmospheric structure is quite nonisothermal. One such example discussed in Part IV, is shown in Fig. 18.

PART II. SECOND METHOD: INVERSION

1. *Review of the Inversion Method*

We now show that the second method of analysis, by formal inversion of the light curve, is the preferable form of analysis, and that it yields good results even in the presence of numerous spikes. Since the method is well-known and has been used in the past by Kovalevsky and Link (1969) and Hubbard *et al.* (1972) as well as by Fjeldbo, Kliore, and Eshleman (1971) for radio occultations, we review it briefly and then show that the algorithm can be used to successfully invert occultation curves dominated by spikes. The uniqueness of solutions found by this method is briefly discussed in Section II-2, as are the effects of random noise.

It should be clear, that, whenever spikes dominate an occultation curve, the inversion method must lead to better results than the curve fitting methods discussed in Part I, because the inversion method uses the information about the atmosphere contained in the spikes. The curve fitting method ignores this information.

In this discussion, it is assumed that spikes are due to small density fluctuations in the vertical structure of the atmosphere as proposed by Freeman and Lyngå (1970). In seeking a solution by inversion it is implicitly assumed that ray crossing is negligible. On this assumption, which amounts to saying that the spikes really occur at the level in the atmosphere indicated by their position on the occultation curve, even very spiky occultation curves can be inverted successfully to yield refractivity profiles. The spikes translate into very small fluctuations in the refractivity profile (Fig. 9), and it is therefore probably true that the inferred refractivity profile is essentially correct even if some of the spikes are due to severe ray crossing. At any rate, in the usual case, there is no way in which ray crossing can be dealt

with, and therefore the assumption that it is negligible is unavoidable.

The total bending of a light ray passing through a spherically symmetric atmosphere is given by equation (1), which may be written as:

$$\theta(r_1) = \int_{-\infty}^{+\infty} K(r)\,dx \qquad (1')$$

where r_1 is the distance of the ray at closest approach from the center of the planet (Fig. 1), and $K(r)$ is the curvature of the ray:

$$K(r) = (1/n)(dn/dr) = (d/dr)(\ln n).$$

We are adopting the assumptions listed, and shown to be valid for a typical stellar occultation, by Baum and Code (1953). A more general treatment, applicable to radio occultations is given by Fjeldbo *et al.* (1971).

From the geometry of Fig. 1,

$$x^2 = r^2 - {r_1}^2$$

and

$$dx = \frac{r\,dr}{(r^2 - {r_1}^2)^{1/2}}$$

Hence Eq. (1′) may be rewritten as:

$$\theta(r_1) = 2\int_{r_1}^{\infty} \frac{r(d/dr)(\ln n)\,dr}{(r^2 - {r_1}^2)^{1/2}}. \qquad (8)$$

The task is to invert this integral equation to yield $n = n(r)$.

Letting ${r_1}^2 = 1/s$ and $r^2 = 1/w$, Eq. (8) becomes:

$$\theta(s) = 2\int_0^s \left(\frac{s}{w}\right)^{1/2} \frac{\psi(w)\,dw}{(s-w)^{1/2}} \qquad (9)$$

where

$$\psi(w) \equiv (w^{1/2}/2)\cdot(d/dw)\cdot\ln(n).$$

Since the major part of the bending of the light ray takes place over only a few scale heights, and since $H \ll r_1$, we can approximate the r in the numerator of the integrand of (8) by r_1, in which case $(s/w)^{1/2} = 1$, and we arrive at an Abel integral equation:

$$\theta(s) = 2\int_0^s \frac{\psi(w)\,dw}{(s-w)^{1/2}} \qquad (10)$$

whose solution is (Bateman, 1910)

$$\psi(w) = \frac{1}{2\pi}\frac{d}{dw}\int_0^w \frac{\theta(s)\,ds}{(w-s)^{1/2}}. \qquad (11)$$

Recalling the definitions of the symbols, we may rewrite this as

$$\frac{d}{dr}(\ln n) = -\frac{1}{\pi} r \frac{d}{dr}\int_r^{\infty} \frac{r\theta(r_1)\,dr}{r_1^2(r_1^2 - r^2)^{1/2}} \qquad (12)$$

and, after some manipulation, simplify to

$$\frac{d}{dr}(\ln n) = -\frac{1}{\pi}\frac{d}{dr}\int_r^{\infty} \frac{\theta(r_1)\,dr}{(r_1^2 - r^2)^{1/2}}. \qquad (13)$$

The conditions which must be satisfied for $\psi(w)$ given by (11) to be a unique solution of (10), and to be continuous in the interval $(0 \leqslant w \leqslant b)$, are given by Bateman (1910). These conditions are satisfied by typical occultation light curves, on the assumption that light rays do not cross.

Allowing the following approximations:

$$K(r) = (1/n)(dn/dr) \simeq dn/dr$$

and $r + r_1 \simeq 2r_1 \simeq 2R_p$ (R_p = planet's radius), Eq. (13) becomes:

$$\frac{dn}{dr} = \frac{-1}{\pi}\frac{1}{(2R_p)^{1/2}}\frac{d}{dr}\int_r^{\infty} \frac{\theta(r_1)dr_1}{(r_1 - r)^{1/2}}. \qquad (13')$$

This integral is negative and its magnitude increases as r decreases. Therefore its derivative with respect to r is positive and dn/dr is negative, as it should be.

It follows from (13′)

$$\nu(r) = \frac{1}{\pi(2R_p)^{1/2}}\int_{\infty}^{r} \frac{\theta(r')\,dr'}{(r' - r)^{1/2}} \qquad (14)$$

where we are now using r' as the dummy variable of integration. Equation (14) is the formal inversion of Eq. (8).

In order to evaluate (14) it is necessary to determine $\theta(r)$ from the light curve data points $\phi(t)$. From the occultation geometry

$$(\phi^*/\phi - 1) = D(\Delta\theta/\Delta r) \qquad (2')$$

and

$$\Delta r + D\Delta\theta = -v\Delta t.$$

Solving this pair of equations for Δr and $\Delta\theta$:

$$\Delta r = -v\Delta t(\phi/\phi^*)$$
$$\Delta\theta = -(1 - \phi/\phi^*)(v\Delta t/D).$$

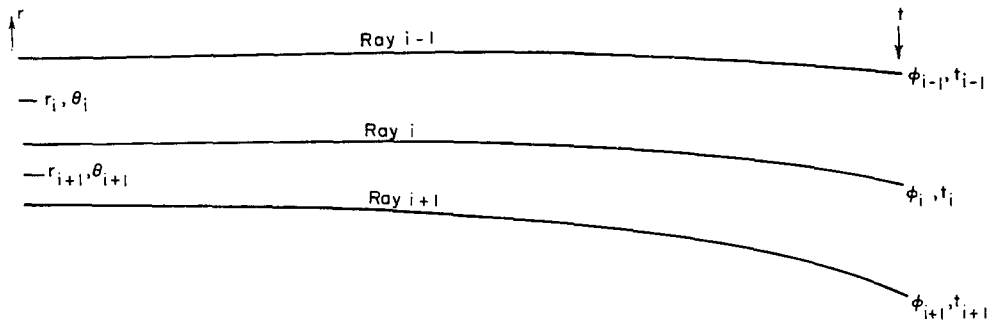

FIG. 8. Schematic ray diagram illustrating how the various $\Delta\theta$'s are obtained from the light curve. (See text for details.)

Referring to Fig. 8, we set:

$$\Delta t_i = t_{i+1} - t_i$$

and

$$\bar{\phi}_i = (\phi_{i+1} + \phi_i)/2.$$

We arbitrarily start the integration at some value of ϕ such that $\phi/\phi^* \simeq 1$ and $\Delta\theta \simeq 0$. At each time increment, we compute $\Delta\theta_i$ and Δr_i. Then,

$$\theta_i = \sum_1^N \Delta\theta_i$$

$$r_i = \sum_1^N \Delta r_i$$

So that we have evaluated θ on N spherical, concentric layers $r_1 > r_2 > r_3 > \ldots r_N$ with $\theta_i = \theta(r_i)$ such that $|\theta_1| < |\theta_2| < |\theta_3| < \ldots |\theta_N|$. Note that r_1 now denotes the uppermost layer, rather than the level of closest approach of a ray.

There are constraints on the practical application of this procedure of determining (θ_i, r_i). Starting too high in the atmosphere will lead to some positive $\Delta\theta$'s (due to noise). The θ sum will be close to zero, and the effect will average out. On the other hand, at the other end of the occultation curve, when the noise level is reached, and occasional values of $\phi/\phi^* < 0$ are encountered, positive values of Δr result, and these are meaningless. Therefore the procedure must be stopped before the noise dominated tail of the occultation light curve is reached.

Since we cannot integrate to infinity in Eq. (14), we must make the approximation

$$\nu(r) \simeq \frac{1}{\pi(2R_p)^{1/2}} \int_{r_1}^{r} \frac{\theta(r')\,dr'}{(r'-r)^{1/2}} \qquad (15)$$

As it stands, Eq. (15) is not suitable for numerical integration since the largest contribution to the integral comes from points close to $r' = r$ where the integrand has a singularity. The equation can be integrated by parts ($du = dr'/(r'-r)^{1/2}$, $v = \theta(r')$) to give

$$\nu(r) = \frac{-2(r_1 - r)^{1/2}\,\theta(r_1)}{\pi(2R_p)^{1/2}} - \frac{1}{\pi(2R_p)^{1/2}} \int_{r_1}^{r} 2(r'-r)^{1/2}\,d\theta$$

Then, the refractivity in the jth shell is

$$\nu_j = \frac{-2(r_1 - r_j)^{1/2}\,\theta_1}{\pi(2R_p)^{1/2}} - \frac{1}{\pi(2R_p)^{1/2}} \sum_{k=1}^{j} (r_k - r_j)^{1/2}(\theta_{k+1} - \theta_{k-1}) \qquad (16)$$

As we have indicated, one would wish to choose $r_1 = \infty$ and $\theta_1 = \theta(r_1) = 0$. But since the occultation light curve does not extend to $r = \infty$, it is necessary to start the integration at some point at which $\theta(r)$ is finite. What is the error produced by this necessary approximation?

Since from (14)

$$\nu(r) = \frac{1}{\pi(2R_p)^{1/2}} \times \left[\int_{r_1}^{r} \frac{\theta(r')\,dr'}{(r'-r)^{1/2}} + \int_{\infty}^{r_1} \frac{\theta(r')\,dr'}{(r'-r)^{1/2}}\right] \qquad (17)$$

stopping the integration at $r = r_1$ means neglecting the second term as we did in Eq. (15). The fractional error in ν resulting from this approximation is given by the ratio of the second term to the first term,

a quantity which we denote by $\epsilon_\nu(r,r_1)$. For an isothermal atmosphere

$$\theta(r') = \theta(r_0)\, e^{-(r'-r_0)/H}$$

where r_0 is some reference level. In this $\epsilon_\nu(r,r_1) = 1 - \text{erf}\,[(r_1 - r)/H]^{1/2}$. Thus for $(r_1 - r) = H$, $2H$, $3H$, and $4H$, $\epsilon_\nu = 16\%$, 5%, 1.5%, and 0.5%, respectively. Hence a valid rule is that all values of $\nu(r)$ determined from (16) for $r_1 - r < 3H$ will have significant errors (r_1 being the starting point of the integration). Neglecting the contribution to the total bending of layers above the level r_1 will have almost no effect on the values of $\nu(r)$ inferred for layers for which $r_1 - r > 3H$.

The method outlined in this section has been successfully used by Hubbard *et al.* (1972) to invert occultation light curves. We only wish to demonstrate that this method works extremely well even in the presence of numerous sharp spikes. In Fig. 9 are shown: (a) an occultation light curve obtained during the May 13, 1971 occultation of β Sco AB by Jupiter; (insert) the inferred refractivity profile obtained using Eq. (16); and (b) the reconstructed light curve generated using this refractivity profile and Eq. (1). The close resemblance between curves (a) and (b) is convincing proof of the power of this method even in the case of very "spiky" light curves.

It should be noted that we always neglect inferred values of $\nu(r)$ for about three scale heights below the starting level r_1, since these values are likely to be vitiated by the assumed starting conditions in Eq. (16). Hubbard *et al.* (1972) have attempted to extract information from this part of the refractivity profile by introducing "corrections". We briefly discuss why we have chosen to avoid such procedures.

By starting the integration at level r_1, the neglected term, E_ν, is given by

$$E_\nu = -\left(\frac{H}{2\pi R_p}\right)^{1/2} \theta_1\, e^{(r_1-r)/H}\left[1 - \text{erf}\left(\frac{r_1 - r}{H}\right)^{1/2}\right]$$

assuming an isothermal atmosphere with scale height H, above the level r_1. This is the second term in Eq. (17).

Hubbard *et al.* (1972) have used such an expression to correct their refractivity profiles. They find H as the best isothermal fit to their refractivity profile using a least squares fit, and θ_1 from the fact that for an isothermal atmosphere.

$$\theta_1 = -(H/D)(\phi^*/\phi_1 - 1)$$

The value of (ϕ^*/ϕ_1) is read from their best isothermal fit at a time corresponding to the first data point used in the inversion. Since (ϕ^*/ϕ_1) is very close to unity ($\sim$0.98), a very small uncertainty in (ϕ^*/ϕ_1) leads to a very large error in θ_1, and hence, in the "correction" E_ν. We have, therefore, chosen not to follow such a procedure.

2. *Solution by Inversion: Effects of Noise*

Since real occultation light curves are subject to noise, its effect on the refractivity profile solutions obtained by the inversion method must be considered. Each increment in θ, $\Delta\theta_i$, depends only on the corresponding flux at that level:

$$\Delta\theta_i = -(v\Delta t/D)(1 - \phi_i/\phi^*)$$

and

$$\theta_n = \sum_1^n \Delta\theta_i,$$

so that for values of ϕ_i/ϕ^* close to unity, the percentage error in $\Delta\theta_i$ is much larger than the corresponding percentage error in ϕ_i/ϕ^*. That is, the values of $\Delta\theta_i$ closest to the top of the occultation curve (those at the beginning of the integration) are the most susceptible to noise fluctuations. Therefore the effects of noise should be most pronounced on the upper portions of inferred refractivity profiles. They will tend to damp out lower down because

$$\nu_j \sim \sum_{k=1}^{j} (r_k - r_j)(\theta_{k+1} - \theta_{k-1})$$

and $\theta_{k+1} - \theta_{k-1} = \Delta\theta_k + \Delta\theta_{k-1}$, so that large errors in the first few values of $\Delta\theta_i$ are summed into all later values of ν_j. Their relative significance will decrease rapidly, as we go deeper and deeper into the atmosphere, since the refractivity, ν, is increasing exponentially.

The effects of noise are difficult to study with any generality, and we restrict our-

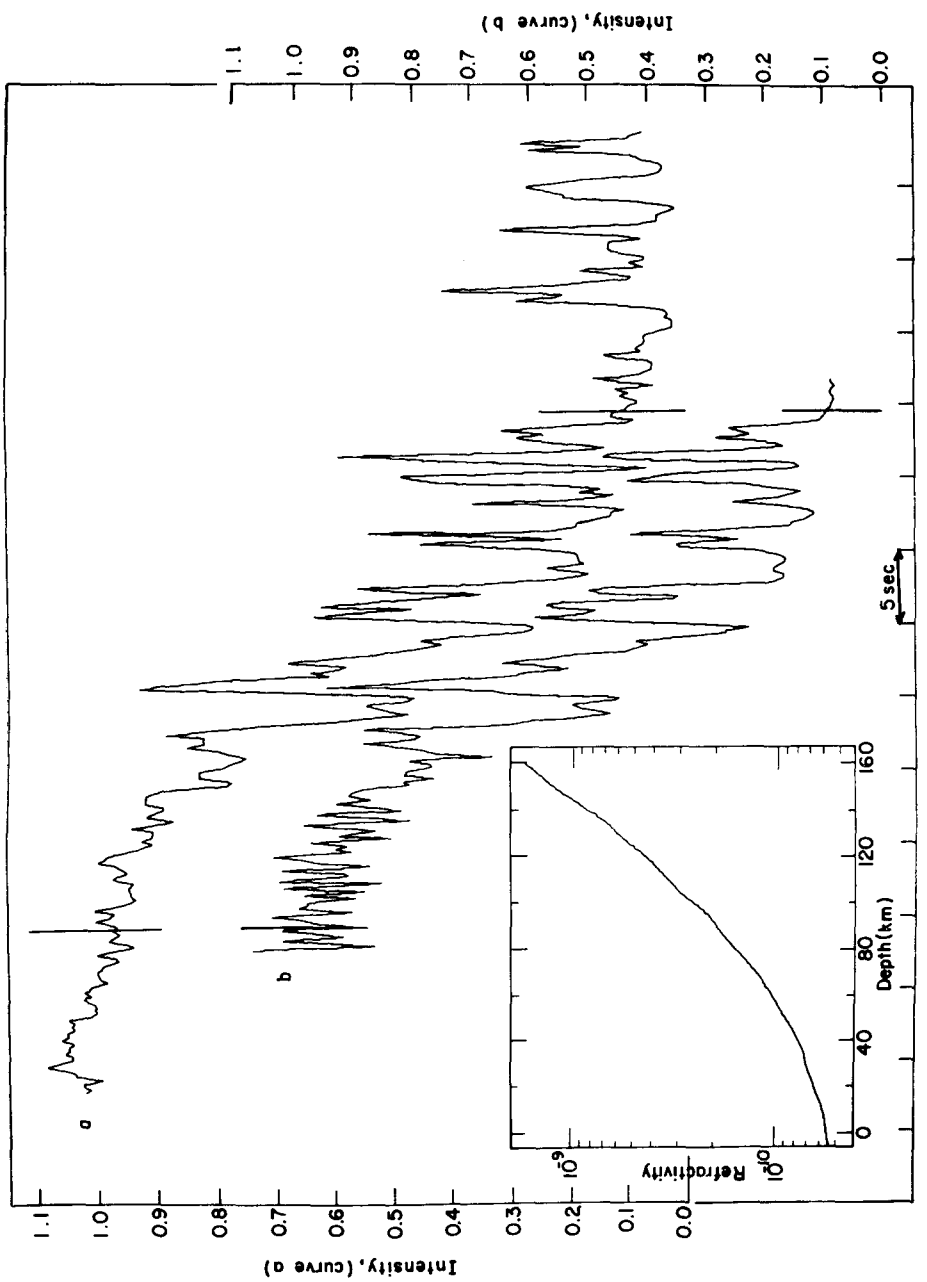

FIG. 9. The insert shows the refractivity profile calculated by inverting curve (a), an occultation light curve obtained during the May 13th, 1971, occultation of β Sco AB by Jupiter. This refractivity profile was used to generate a synthetic light curve (b), which closely matches the observed curve. Note that the small wiggles in the refractivity profile correspond to the spikes in the light curve.

selves to a few specific examples to get a feeling for the situation:

A. A constant gradient atmosphere, $G = 0.1$, $H_0 = 25$km, $v = 7.5$km/sec. No noise.

B. Same as (A), but with 3% random noise.

C. An isothermal atmosphere, $H = 20.02$ km and $v = 7.5$km/sec. No noise.

D. Same as (C), but with 3% random noise.

The light curves are shown in Figs. 10 and 11. The isothermal atmosphere chosen is that whose light curve provides the best fit to the constant gradient atmosphere (A) with the constraint that for both curves $t = 0$ at $\phi^*/\phi = 2$, i.e., $t_0 = 0$. This fit differs from that in Fig. 5 because the constraints are different.

The refractivity profiles, obtained by the inversion technique described in Section II–1, are compared with the true profiles in Figs. 12 and 13. Representative values are tabulated in Tables IV and V. The actual values of ν shown are obtained from the equation:

$$\nu = \nu_0 \left[1 + \frac{G}{H_0}(r - r_0)\right]^{-\frac{1}{G}-1} \qquad (18)$$

where:

$$\nu_0 = \frac{{H_0}^2}{D\left(\frac{2H_0 R_p}{G}\right)^{1/2}(1+G)(1+\frac{3}{2}G)\,B\left(\frac{1}{2}, \frac{1}{G}+\frac{3}{2}\right)} \qquad (18)$$

Here, B is the Beta Function. In our case $1/G = 10$, and $B = 0.5284$. The value of D used was that corresponding to the distance of Jupiter on May 13, 1971 (6.538×10^8 km). For $G = 0$ equation (18) reduces to

$$\nu = \nu_0 e^{-(r-r_0)/H} \qquad (19)$$
$$\nu_0 = (H/D)(H/2\pi R_p)^{1/2},$$

and H is the isothermal scale height.

In both cases in the absence of noise the calculated values of ν approach the true refractivity profile from below since we are neglecting contributions from the uppermost layers of the atmosphere. The effect of 3% noise for the isothermal case appears as an additive factor of about 7×10^{-13} in the refractivity at the beginning of the integration. Although this effect quickly becomes negligible, it does significantly affect the slope of the refractivity profile for about the first 100km. The noise is somewhat smaller in the linear gradient case and damps out faster, although it is

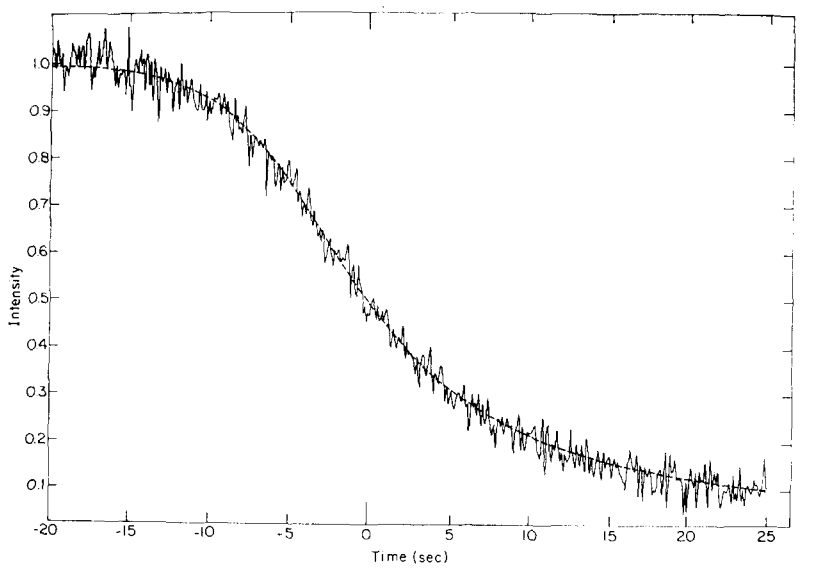

FIG. 10. The light curves for a constant gradient atmosphere $G = 0.1$, $H_0 = 25$km, with no noise (dashed) and with 3% random noise (solid). A value of $v = 7.5$km/sec is assumed, typical for a Jovian occultation.

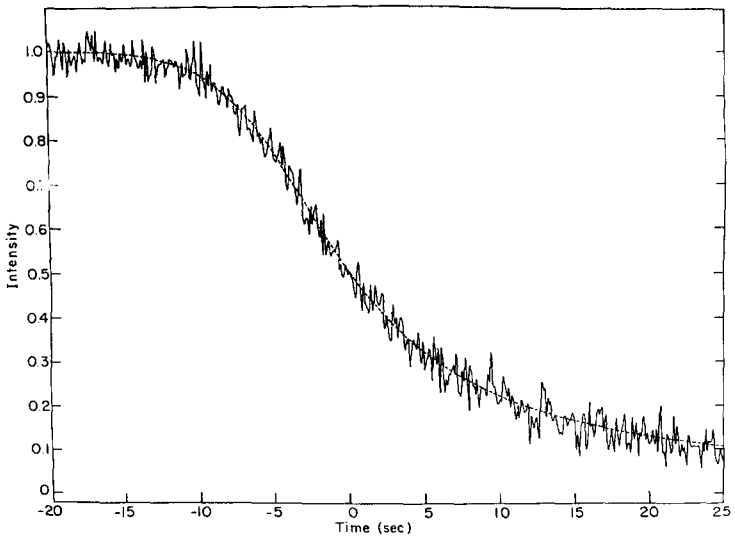

FIG. 11. The curves for an isothermal atmosphere $H = 20.02$km, with no noise added (dashed), and with 3% random noise (solid). The value of v is that used in Fig. 10.

important to note that the specific effects of noise are only illustrative since we are examining only one of an infinite number of possibilities.

The conclusion to be drawn from this exercise is that if the first three scale heights of the refractivity profile are ignored (as suggested in Section II-1), then, even in the presence of reasonable amounts of noise, faithful refractivity profiles can be obtained by the inversion method. High quality observed light curves should have less than 3% noise.

It should be noted from Figs. 12 and 13 that, even in the presence of 3% noise, the linear temperature gradient atmosphere *can* be distinguished from the isothermal one. In the former case, at the deepest levels, the refractivity profile is nonlinear and concave upwards; in the second case

TABLE IV

SELECTED REFRACTIVITY VALUES FROM FIGURE 12[a]

r (km)	ϕ/ϕ^*	Actual ν (Eq. 18)	Inversion ν	
			No noise	3% Noise
30.1	0.985	6.17 (−12)	2.35 (−12)	2.84 (−12)
50.0	0.975	1.18 (−11)	7.32 (−12)	7.25 (−12)
75.3	0.91	2.83 (−11)	2.33 (−11)	2.47 (−11)
100.1	0.79	7.24 (−11)	6.75 (−11)	7.20 (−11)
129.1	0.50	2.42 (−10)	2.40 (−10)	2.53 (−11)
150.1	0.25	6.37 (−10)	6.44 (−10)	6.65 (−10)
165.2	0.10	1.35 (−9)	1.37 (−9)	—

[a] In the last three columns each number is to be multiplied by the power of ten indicated within the brackets.

TABLE V

SELECTED REFRACTIVITY VALUES FROM FIGURE 13[a]

r (km)	ϕ/ϕ^*	Actual ν (Eq. 19)	Inversion ν	
			No noise	3% noise
25.3	0.99	1.07 (−12)	4.64 (−13)	1.34 (−12)
50.2	0.98	3.72 (−12)	2.84 (−12)	4.77 (−12)
75.1	0.94	1.29 (−11)	1.19 (−11)	1.57 (−11)
100.4	0.81	4.56 (−11)	4.50 (−11)	4.96 (−11)
130.6	0.50	2.07 (−10)	2.10 (−10)	2.15 (−10)
150.2	0.27	5.48 (−10)	5.59 (−10)	5.73 (−10)
168.2	0.10	1.35 (−9)	1.38 (−9)	—

[a] In the last three columns each number is to be multiplied by the power of ten indicated within the brackets.

the profile is linear at these levels. This is significant since the isothermal atmosphere was chosen to have a light curve as close as possible to that of the linear gradient atmosphere with the constraint that they both pass through $t = 0$ at $\phi/\phi^* = 0.5$. As pointed out previously, this gives a slightly different fit than that in Fig. 5, where we have not imposed any constraints on the fit.

PART III. TEMPERATURE PROFILES

1. *Deriving Temperature Profiles from Refractivity Profiles*

To generate temperature profiles from refractivity profiles, refractivities must first be converted into densities. Assuming a constant mean molecular weight:

$$\rho(r) = (\rho_s/\nu_s)\,\nu(r) \tag{20}$$

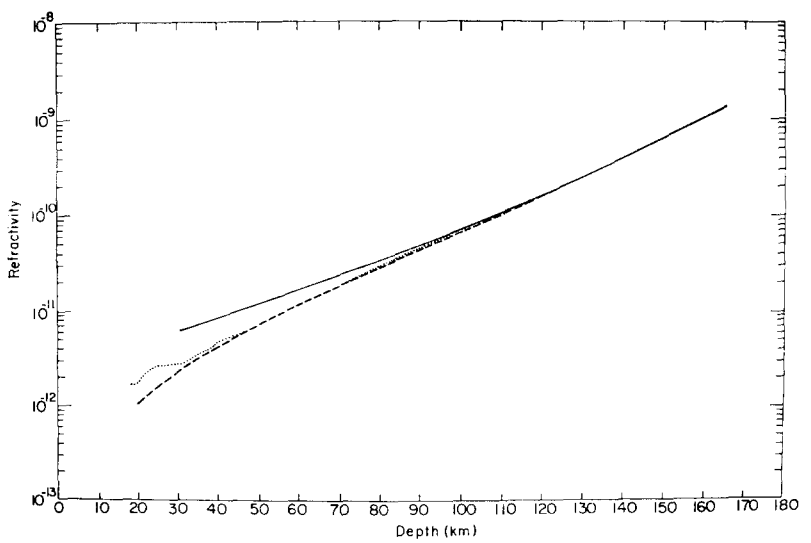

FIG. 12. Refractivity profiles obtained by inverting the light curves shown in Fig. 10 compared with the true refractivity profile (solid). The inverted profiles correspond to the cases of no random noise added (dashed), and to 3% random noise added (dotted). (See Fig. 10.)

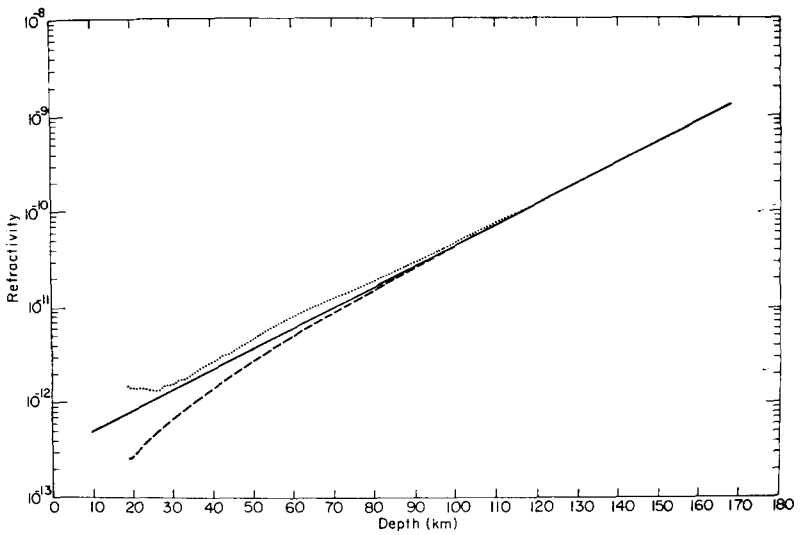

FIG. 13. Refractivity profiles obtained by inverting the light curves shown in Fig. 11 compared with the true refractivity profile (solid). The inverted profiles correspond to the cases of no random noise added (dashed), and to 3% random noise added (dotted). (See Fig. 11.)

where the subscript s refers to STP conditions and:

$$\rho_s = \mu m_H L \tag{21}$$

where m_H = mass of a hydrogen atom and L = Loschmidt's number.

To proceed we must specify the composition of the atmosphere. Since most recent occultations have involved the outer planets, we shall couch our discussion in terms of hydrogen–helium atmospheres.

For such atmospheres, the refractivity at STP is given by

$$\nu_s = f_{\mathrm{He}}(\nu_s)_{\mathrm{He}} + f_{\mathrm{H_2}}(\nu_s)_{\mathrm{H_2}},$$

where f_{He} = helium fraction by number = $\mu/2 - 1$ and $f_{\mathrm{H_2}}$ = hydrogen fraction by number = $1 - f_{\mathrm{He}}$. The refractivities of hydrogen and helium at STP can be represented with sufficient accuracy for present purposes by

$$(\nu_s)_{\mathrm{He}} = A_{\mathrm{He}}\left(1 + \frac{B_{\mathrm{He}}}{\lambda^2}\right),$$

and

$$(\nu_s)_{\mathrm{H_2}} = A_{\mathrm{H_2}}\left(1 + \frac{B_{\mathrm{H_2}}}{\lambda^2}\right)$$

where the wavelength λ is in micrometers and the dispersion constants according to Allen (1963) are $A_{\mathrm{He}} = 3.48 \times 10^{-5}$, $B_{\mathrm{He}} = 2.3 \times 10^{-3}$, $A_{\mathrm{H_2}} = 13.58 \times 10^{-5}$, and $B_{\mathrm{H_2}} = 7.52 \times 10^{-3}$.

Once f_{He} or $f_{\mathrm{H_2}}$ is specified, the refractivity profile can be converted into a density profile using the formulas above.

2. *Algorithm for Deriving Temperature Profiles*

The temperature profile can be derived from the density profile using the perfect gas law and the equation of hydrostatic equilibrium. Divide the atmosphere into N plane parallel layers, numbered downward 1 to N. Choose P_1 to be small, but arbitrary. The values of $\rho_1, \rho_2, \ldots \rho_N$ are known from above, and the temperature structure can be found from:

$$\begin{aligned} \bar{\rho}_i &= (\rho_i + \rho_{i+1})/2, \\ dP_i &= -\bar{\rho}_i g \Delta r, \\ P_{i+1} &= \sum_1^i dP_i + P_1, \\ T_{i+1} &= \frac{\mu m_H P_{i+1}}{k\rho_{i+1}}. \end{aligned} \tag{22}$$

It is clear that in the uppermost layers the temperature derived will depend significantly on the boundary condition: P_1. However, for $P_i \gg P_1$ this influence

should become negligible. This is illustrated in the following section where the convergence properties of the algorithm in the case of a linear temperature gradient atmosphere are studied.

3. *Convergence of the Temperature Algorithm in the Special Case of a Linear Temperature Gradient Atmosphere*

For a linear temperature gradient atmosphere (Goldsmith, 1963)

$$\rho = \rho_0 \left[1 + \frac{G}{H_0}(r - r_0)\right]^{-\gamma - 1} \tag{23}$$

where the subscript zero refers to the level at which $\phi^*/\phi = 2$, $H = H_0$; also $\gamma = 1/G$. The pressure as a function of height is given by

$$P(r) = P_1 - \int_{r_1}^{r} \rho g \, dr$$

where P_1 is the assumed pressure at the boundary $r = r_1$. Substituting (23) and integrating:

$$P(r) = P_1 + \rho_0 H_0 g \left(\left[1 + \frac{G}{H_0}(r - r_0)\right]^{-\gamma} - \left[1 + \frac{G}{H_0}(r_1 - r_0)\right]^{-\gamma}\right) \tag{24}$$

which, using the perfect gas law, gives

$$T(r) = \frac{\mu m_H P_1}{k\rho} + \frac{\rho_0 g H_0 \mu m_H}{k\rho} \times \left(\left[1 + \frac{G}{H_0}(r - r_0)\right]^{-\gamma} - \left[1 + \frac{G}{H_0}(r_1 - r_0)\right]^{-\gamma}\right) \tag{25}$$

and eliminating ρ by using (23), we finally have:

$$T(r) = \frac{g H_0 \mu m_H}{k} \times \left[1 + \frac{G}{H_0}(r - r_0)\right] + \left[1 + \frac{G}{H_0}(r - r_0)\right]^{\gamma + 1} \times \left(\frac{\mu m_H P_1}{k\rho_0} - \frac{g H_0 \mu m_H}{k}\left[1 + \frac{G}{H_0}(r_1 - r_0)\right]^{-\gamma}\right) \tag{26}$$

Recall that P_1 represents the assumed boundary value of the pressure, and say that the true value is $P_1{}^t$, so that

$$P_1 = A \cdot P_1{}^t \tag{27}$$

where A is a constant. Since:

$$P_1{}^t = P_0[1 + (G/H_0)(r_1 - r_0)]^{-\gamma},$$
$$T_0 = g H_0 \mu m_H / k,$$
$$dT/dr = T_0(G/H_0) = gG\mu m_H/k,$$

and $P_0 = (\rho_0/\mu m_H) k T_0$, Eq. (26) may be rewritten in the form:

$$T(r) = T_0 + \frac{dT}{dr}(r - r_0) + \left[1 + \frac{G}{H_0}(r - r_0)\right]^{\gamma + 1} \times \left[1 + \frac{G}{H_0}(r_1 - r_0)\right]^{-\gamma} (A - 1)\, T_0 \tag{28}$$

which gives the temperature profile inferred in terms of the error factor A [Eq. (27)]. When $A = 1$, Eq. (28) reduces, as it should, to:

$$T(r) = T_0 + (dT/dr)(r - r_0) \tag{29}$$

Equation (28) can now be used to study the effects of the pressure boundary condition at r_1 on the inferred temperature profile. The problem cannot be pursued in total generality and we consider only two illustrative examples for the case $A = 0$. This choice for A is reasonable since the usual assumption is that $P_1 = 0$ at $r = r_1$.

Table VI shows the results of these calculations for atmospheres having $T_0 = 150°\text{K}$ and $G = +0.1$ and -0.1 respectively. Note that in this case, $r - r_0$ is related to ϕ (the light curve flux) by:

$$(r - r_0)/H = \gamma\,[(\phi^*/\phi - 1)^{-1/(\gamma + 5/2)} - 1]. \tag{30}$$

If in practice $r = r_1$ is taken to correspond to the $\phi = 0.98\phi^*$ level, then for $G = +0.1$, $r_1 - r_0 = 3.7\ H_0$. For $G = -0.1$, the value is $4.1\ H_0$. Recall that r_0 is the level for which $\phi = 0.50\phi^*$.

It is clear from Table VI that the temperature profile does not begin to converge to the correct value until after three scale heights from the upper boundary. Below r_0, convergence is rapid in both cases.

For an isothermal atmosphere ($G = 0$) Eq. (28) becomes

$$T(r) = T_0[1 + (A - 1)\, e^{(r - r_1)/H}] \tag{31}$$

TABLE VI

CONVERGENCE OF TEMPERATURE ALGORITHM FOR TWO LINEAR TEMPERATURE GRADIENT MODEL ATMOSPHERES[a]

	$G = +0.1$			$G = -0.1$		
$r - r_0$	T (true)	T (Eq. 28)	% error	T (true)	T (Eq. 28)	% error
$4H_0$	—	—	—	90	13.5	85
$3H_0$	195	79.5	59.2	105	85.5	18.6
$2H_0$	180	132.0	26.7	120	114.3	4.8
H_0	165	147.0	10.9	135	133.0	1.5
0	150	143.5	4.3	150	149.2	0.5
$-H_0$	135	133.0	1.5	165	164.7	0.2
$-2H_0$	120	119.4	0.5	180	179.9	0.06

[a] See text for details.

and (30) reduces to:

$$(r - r_0)/H = -\ln(\phi^*/\phi - 1)$$

and $\phi = 0.98\phi^*$ corresponds to $(r_1 - r_0) = 3.9\,H$, so that:

$$T(r) = T_0[1 + (A - 1)\,e^{-3.9}\,e^{(r-r_0)/H}]. \quad (32)$$

The convergence properties for $T_0 = 150°$ and $A = 0$ are shown in Table VII. Again, for about three scale heights from the top convergence is poor, but becomes satisfactory below $r = r_0$.

We wish to stress that the above examples should only be considered as illustrative. The convergence properties depend on the specific choice of A, G and on the initial ϕ value (i.e., r_1). For instance, we have not proven that the trend evident in the above examples, that $G < 0$ converges faster than $G = 0$, which in turn converges faster than $G > 0$, is always true. Note, however, that our results are independent of the scale height H, and that the percent error in T given in Tables VI and VII must be independent of T_0 since it can be factored out of Eq. (28) and (31).

TABLE VII

CONVERGENCE OF TEMPERATURE ALGORITHM FOR AN ISOTHERMAL MODEL ATMOSPHERE[a]

$r - r_0$	T (true)	T (Eq. 32)	% error
$3H$	150	88.5	41
$2H$	150	127.5	15
H	150	141.8	5.5
0	150	147.0	2.0
$-H$	150	148.9	0.73
$-2H$	150	149.6	0.27

[a] See text for details.

4. *Practical Applications of the Temperature Algorithm*

The algorithm discussed in the two preceding sections can be modified slightly in practice. The initial boundary condition $P_1 = 0$ at $r = r_1$ implies $T_1 = 0$ which is certainly not correct. By fitting a straight line to the quasi-linear portion of refractivity profiles (such as those shown in Figs. 12 and 13) an approximate scale height $\tilde{H}$ can be obtained.

After one iteration, if the inferred pressure at level N is P_N (using $P_1 = 0$), the next iteration can begin with

$$P_1 = P_N e^{-(r_1 - r_N)/\tilde{H}}$$

or alternately, $\tilde{H}$ can be used to estimate the initial temperature T_1. Thus successive iterations are possible, with a new P_1 being determined each time using $\tilde{H}$. This process converges rapidly. We refer to this method as Method A in what follows.

A related procedure for determining $T(r)$ was suggested by Hubbard *et al.*

(1972). From the perfect gas law:

$$dP = (k/\mu m_H)(T\,d\rho + \rho dT)$$

which, when combined with the equation of hydrostatic equilibrium, gives

$$H\left(\frac{1}{\rho}\frac{d\rho}{dr} + \frac{1}{T}\frac{dT}{dr}\right) = -1 \qquad (33)$$

Defining a density scale height H_* by the equation,

$$\frac{1}{H_*} \equiv \frac{-1}{\rho}\frac{d\rho}{dr},$$

Eq. (33) becomes

$$-\frac{dH}{dr} + \frac{H}{H_*} = 1 \qquad (34)$$

Assuming constant composition, we have

$$\frac{1}{H_*} = \frac{-1}{\rho}\frac{d\rho}{dr} = \frac{-1}{\nu}\frac{d\nu}{dr},$$

and the refractivity profile gives $H_*(r)$. Given an initial assumption for H_1 (as discussed above), Eq. (34) can be integrated numerically to give $H(r)$, and hence $T(r)$, if a value of μ is assumed. This procedure we call Method B. It should be clear that Methods A and B are conceptually equivalent. They both depend on estimating the scale height at the beginning of the occultation curve—a most uncertain enterprise.

The methods discussed above can now be tested by inverting the refractivity profiles shown in Figs. 12 and 13. In each case we need to estimate the quasiscale height $\tilde{H}$, obtained by fitting straight lines to the quasilinear portions of the refractivity profiles in Figs. 12 and 13. The resulting values of $\tilde{H}$ are given in Table VIII. Note that $\tilde{H}$ departs from H in the third case, even though the noise level is zero, because the refractivity profile generated is not exactly isothermal at the beginning of the integration. This difficulty, discussed in Section II–I, is related to the assumption that no light ray bending occurs above the first point of integration.

The temperature profiles generated by Methods A and B are compared with the true temperature structures for no noise in Figs. 14 and 15; the resulting profiles in the presence of 3% noise are shown in Figs. 16 and 17. The following important points emerge:

1. For about the first four scale heights (depths $\lesssim 100$ km) neither method gives reliable results.

2. More than four scale heights below the starting point (depths $\gtrsim 100$ km) both methods give reasonable and quite comparable results.

3. The integration was stopped at a level corresponding to $\phi = 0.1\phi^*$. At that point neither method had converged to precisely the correct temperature profile.

TABLE VIII

VALUES OF THE QUASISCALE HEIGHT $\tilde{H}$ OBTAINED FROM FIGURES 12 AND 13[a]

Case	Figure	Range fitted (km)	Quasiscale height $\tilde{H}$ (km)
$G = 0.1$, $H_0 = 25$ km (no noise)	Fig. 12 (dashed line)	60–180	23.4
$G = 0.1$, $H_0 = 25$ km (3% noise)	Fig. 12 (dotted line)	60–180	19.3
$G = 0$, $H = 20.02$ km (no noise)	Fig. 13 (dashed line)	80–180	23.0
$G = 0$, $H = 20.02$ km (3% noise)	Fig. 13 (dotted line)	80–180	21.9

[a] See text for details.

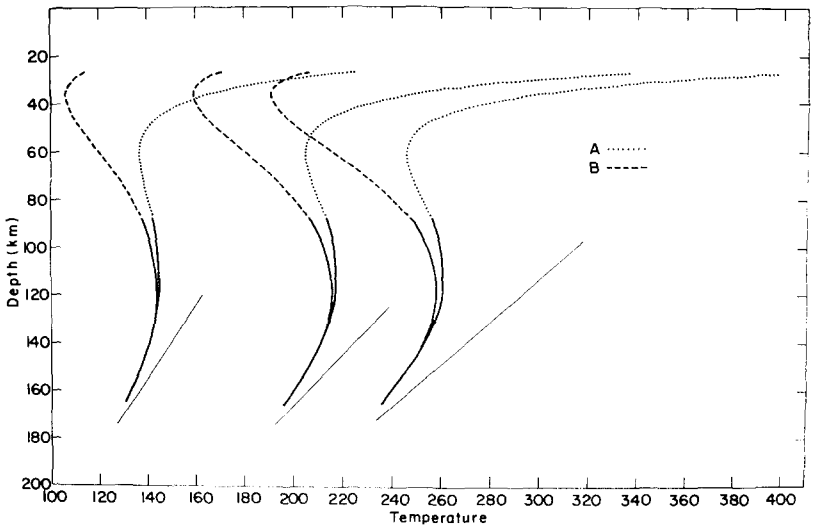

FIG. 14. Temperature profiles calculated by Methods A and B from the refractivity profile in Fig. 12 (no noise). Shown left to right are three cases corresponding to compositions of (1) 100% H_2, 0% He. (2) 50% H_2, 50% He, and (3) 20% H_2, 80% He. In each case, the true atmospheric temperature profile has been sketched in.

4. Moderate amounts of noise (3% in this case) do not have a significant effect on the results.

The difference between the calculated and true temperature profiles can be attributed to three major factors:

1. Errors in the refractivity profile introduced during the light curve inversion. These are especially important near the top of the refractivity profile (Section II–I).

2. Errors in estimating $\tilde{H}$.

3. Errors due to random noise.

Note that either Method A or Method B would give *exactly* accurate temperature profiles everywhere if applied to an *exactly* isothermal refractivity profile. In that case $\tilde{H}$ would equal H. This does not occur in the case of the "no noise" refrac-

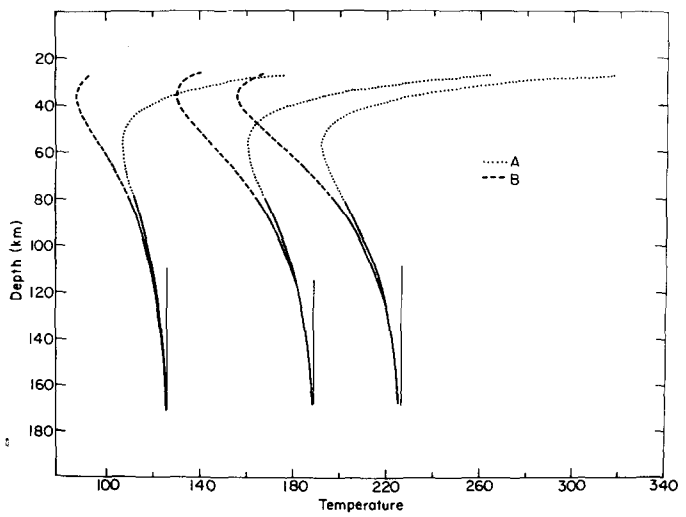

FIG. 15. Same as Fig. 14 but for the dashed refractivity profile in Fig. 13 (no noise).

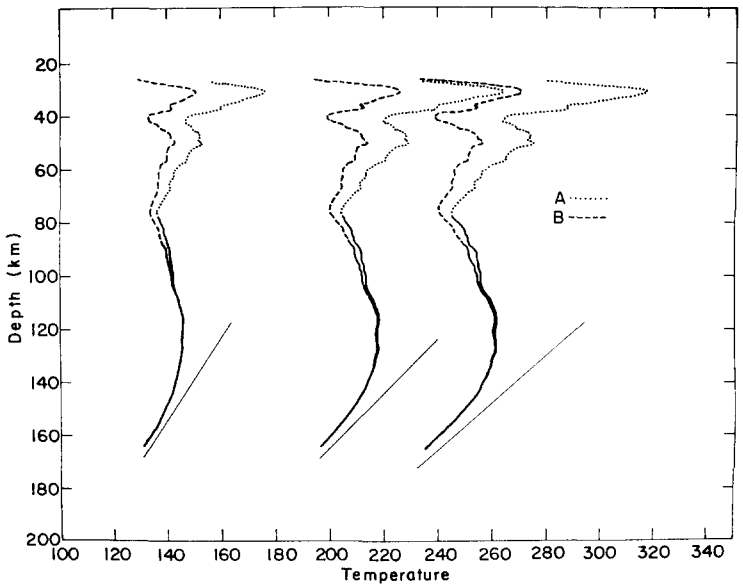

FIG. 16. Same as Fig. 14 but for the dotted refractivity profile in Fig. 12 (3% noise).

tivity profile shown in Fig. 13 used to generate the temperature profiles in Fig. 15, since that profile is not truly isothermal due to inversion errors as explained above.

Even in the case of an *exact* linear gradient refractivity profile, neither Method A nor Method B would give exactly accurate temperature profiles near the beginning of the integration, since, in this case, $\tilde{H}$ would be approximate.

In practice, the procedure is subject to the three errors enumerated above, and inferred temperature profiles cannot be trusted for at least four scale heights from the beginning of the integration. This point is well illustrated in Figs. 15 and 17, where

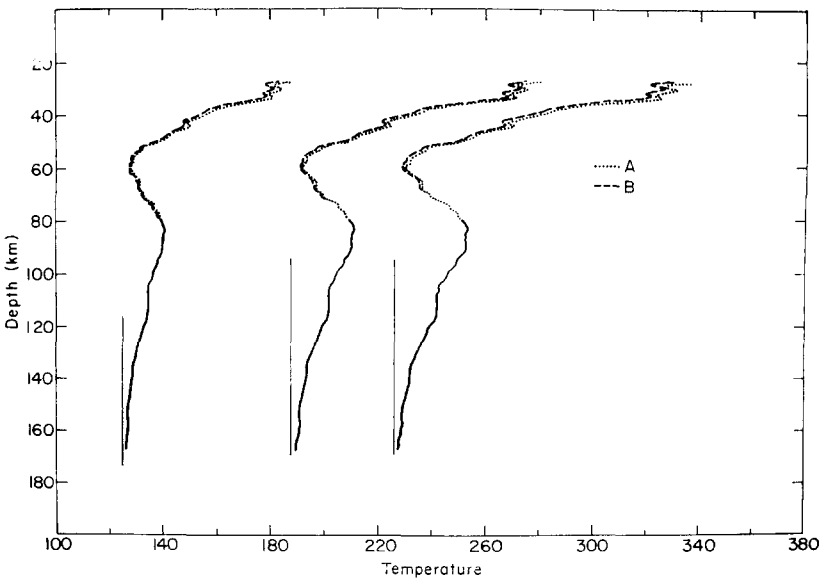

FIG. 17. Same as Fig. 14 but for the dotted refractivity profile in Fig. 13 (3% noise).

it is seen that the effect of noise on the isothermal case is to change the direction from which the solutions converge to the true temperature profile. In neither case, "no noise" and "3% noise," would it be correct to infer a temperature gradient in the region between 100 and 170km (Figs. 15 and 17).

In Figs. 14 and 16, the solutions suggest a quasi-isothermal region between 100 and 130km, which, of course, is not real. However, by the time that the 100km level is reached, the temperature algorithms have correctly converged to the refractivity profiles being used (Fig. 12). Unfortunately, these refractivity profiles are not exactly those of a constant temperature gradient atmosphere, and this error in the refractivity profiles is propagated into the temperature profiles. Specifically, for the $G = 0.1$ atmosphere, the true refractivity profile must be concave upwards everywhere, on a plot such as that shown in Fig. 12. However, starting the inversion at a finite level makes the beginning part of the refractivity profile concave downward. There must then be a quasilinear transition region which will appear in the temperature profile as a quasiisothermal portion.

The conclusion of this section is that no matter how clever an algorithm is used to derive temperatures from refractivity profiles, errors in the refractivity profiles will propagate into the temperature calculations. It was shown in Section II–I that calculated refractivity profiles do not converge to the real values for about three scale heights from the beginning level of the calculation. The situation will therefore be even worse for the temperature profiles. One must be especially cautious of large temperature gradients and fluctuations indicated in the initial portions of temperature profiles (Figs. 14 and 17). However, it appears that more than the three to four scale heights below the beginning of the integration reasonably accurate temperature profiles can be inferred from occultation light curves.

A note of caution is required at this point. Even though spikes translate into small fluctuations in the refractivity profiles, they produce significant fluctuations in the temperature profiles. If ray crossing is severe, the bumps in the temperature profile corresponding to spikes will not only appear at the wrong level but will be wrong in magnitude. All that can be said is that, if most spikes in a light curve do not involve severe ray crossing, the fine structure of the temperature profile will be essentially correct. Otherwise, it will not. As stressed previously, from a single intensity record of an occultation it is impossible to determine whether or not ray crossing occurred.

Part IV. Cases of Variable Molecular Weight

So far we have assumed that the mean molecular weight of the atmosphere is constant in the region sampled by the occultation curve. However, in practice, the occultation curve may start in the region above the turbopause where μ is controlled by diffusive separation and terminate in the layer below the turbopause where μ is constant and the atmosphere is well-mixed. Unfortunately, there appears to be no way of telling from the shape of an occultation light curve whether the region being sampled is above, below, or straddling the turbopause. We wish to prove this assertion with one specific example.

Consider the following idealized case, of an occultation by a planet like Jupiter. Assume that the turbopause occurs at a number density of $n = 3 \times 10^{13}\,\mathrm{cm}^{-3}$, and that the hydrogen–helium atmosphere is isothermal at $T = 100°\mathrm{K}$ below the turbopause and $\mu = 3$. Above the turbopause, the temperature increases linearly at 1.88°K/km, and μ is determined by diffusive separation.

The resulting occultation curve is shown in Fig. 18. The corresponding physical parameters of the atmosphere at various levels are given in Table IX. In that table, H^* is the instantaneous scale height at a given level determined by the equation $H^*(r) = kT(r)/(\mu(r)g(r)m_H)$. Also shown in Fig. 18 is the best isothermal fit ($H_i = 10.03\,\mathrm{km}$) assuming constant μ. Even in

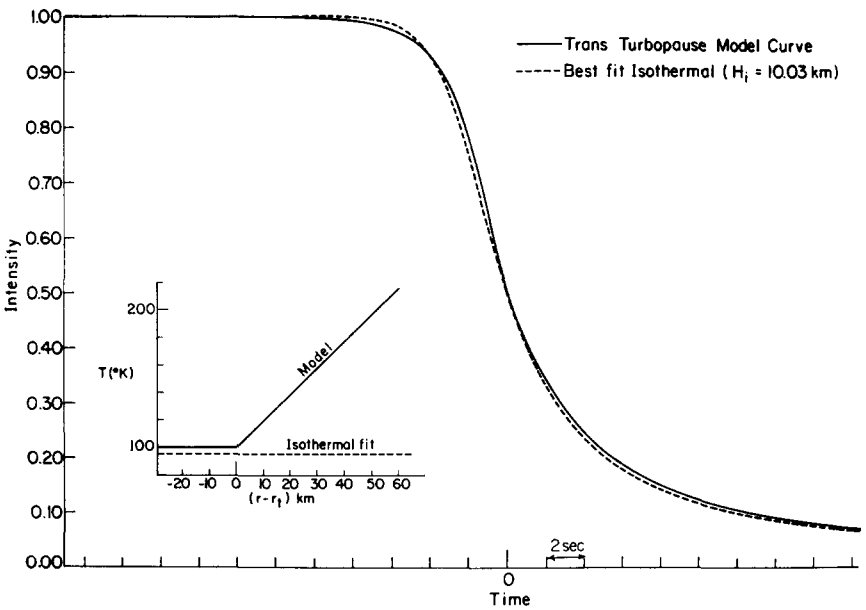

FIG. 18. Occultation curve for an atmosphere in which the mean molecular weight varies with height (see text and Table IX for details). Also shown is the best isothermal fit assuming a constant molecular weight. Shown in the insert is a comparison of the true model temperature profile with that given by the best isothermal (constant μ) fit.

the absence of noise it is almost impossible to tell that the turbopause is crossed at the $\phi/\phi^* = 0.5$ level, and that the atmosphere is not close to isothermal!

A method of determining the mean molecular weight, μ, directly from the arrival times of spikes at several wavelengths has been suggested by Brinkmann (Brinkmann, 1971; Wasserman and Veverka, 1973). If a large number of spikes were observed in a light curve simultaneously at several wavelengths with a time resolution of about 0.01 sec, the constant μ hypothesis could be tested.

In the meantime, it seems best to adopt an indirect approach. From the occultation light curve the number density at the various ϕ levels can be estimated. Atmospheric models can then be used to predict the turbopause level. If the predictions indicate that most of the light curve corresponds to levels below the turbopause,

TABLE IX

ATMOSPHERIC MODEL CORRESPONDING TO FIGURE 18[a]

ϕ/ϕ^*	$(r - r_t)$ (km)	μ	T (°K)	H^* (km)
$\leqslant 0.45$	$\leqslant 0$	3	100	10.6
0.73	10	2.65	119	14.0
0.88	20	2.46	138	17.8
0.94	30	2.33	157	21.4
0.97	40	2.25	176	24.9
0.98	50	2.19	195	28.4
0.99	60	2.14	214	31.8

[a] The turbopause level is denoted by r_t.

the constant μ assumption is justified. Otherwise, the problem becomes intractable, barring the input of additional information.

Acknowledgments

We are particularly grateful to R. T. Brinkmann and an anonymous referee for helpful comments. This research was supported in part by the Atmospheric Sciences Section of the National Science Foundation Grant GA 23945 and in part by NASA Grant NGR-33-010-082.

References

Allen, C. W. (1963). "Astrophysical Quantities," p. 87. The Athlone Press, London, England.

Bateman, H. (1910). The solution of the integral equation connecting the velocity of propagation of an earthquake-wave in the interior of the earth with the times which the disturbance takes to travel to the different stations on the earth's surface. *Phil. Mag. Suppl.* (6) **19**, 576–587.

Baum, W. A., and Code, A. D. (1953). A photometric observation of the occultation of σ Arietis by Jupiter. *Astron. J.* **58**, 108–112.

Brinkmann, R. T. (1971). Occultation by Jupiter. *Nature (London)* **230**, 515–516.

Fjeldbo, G., Kliore, A. J., and Eshleman, V. R. (1971). The neutral atmosphere of Venus as studied with the Mariner V radio occultation experiments. *Astron. J.* **76**, 123–140.

Freeman, K. C., and Lyngå, G. (1970). Data for Neptune from occultation observations. *Astrophys. J.* **160**, 767–780.

Freeman, K. C., and Stokes, N. R. (1972). The occultation of β Sco by Jupiter. *Icarus* **17**, 198–201.

Goldsmith, D. W. (1963). Differential refraction in planetary atmospheres with linear scale height gradients. *Icarus* **2**, 341–349.

Hubbard, W. B., Nather, R. E., Evans, D. S., Tull, R. G., Wells, D. C., van Citters, G. W., Warner, B., and Vanden Bout, P. (1972). The occultation of Beta Scorpii by Jupiter and Io. I. Jupiter. *Astron. J.* **77**, 41–59.

Kovalevsky, J., and Link, F. (1969). Diamètre, aplatissement et propriétés optiques de la haute atmosphère de Neptune d'après l'occultation de l'étoile BD-17° 4388. *Astron. Astrophys.* **2**, 398–412.

Larson, S. M. (1972). Photographic observations of the occultation of Beta Scorpii by Jupiter. Contributions from the Bosscha Observatory. No. 45.

de Vaucouleurs, G., and Menzel, D. H. (1960). Results of the occultation of Regulus by Venus, July 7, 1959. *Nature (London)* **188**, 28–33.

Veverka, J., Elliot, J. L., Liller, W., Sagan, C., and Wasserman, L. (1971). Three channel observations of the occultation of Beta Scorpii by Jupiter. *Bull. Amer. Astron. Soc.* **3**, 374.

Wasserman, L., and Veverka, J. (1973). Analysis of spikes in occultation curves: A critique of Brinkmann's method. *Icarus* **18**, 599–604.